Continuous monitoring of nightside upper thermospheric mass densities in the martian southern hemisphere over 4 martian years using electron reflectometry

Robert J. Lillis [a],[*], Stephen W. Bougher [b], David L. Mitchell [a], David A. Brain [a], Robert P. Lin [a], Mario H. Acuña [c]

[a] *UC Berkeley Space Sciences Laboratory, 7 Gauss Way, Berkeley, CA 94720, USA*
[b] *University of Michigan Department of Atmospheric, Oceanic and Space Sciences, 2455 Hayward St., Ann Arbor, MI 48109-2143, USA*
[c] *NASA Goddard Space Flight Center, Greenbelt, MD 20771, USA*

Abstract

Details are presented of an improved technique to use atmospheric absorption of magnetically reflecting solar wind electrons to constrain neutral mass densities in the nightside martian upper thermosphere. The helical motion of electrons on converging magnetic field lines, through an extended neutral atmosphere, is modeled to enable prediction of loss cone pitch angle distributions measured by the Magnetometer/Electron Reflectometer (MAG/ER) experiment on Mars Global Surveyor at 400 km altitude. Over the small fraction of Mars' southern hemisphere (∼2.5%) where the permanent crustal magnetic fields are both open to the solar wind and sufficiently strong as to dominate the variable induced martian magnetotail field, spherical harmonic expansions of the crustal fields are used to prescribe the magnetic field along the electron's path, allowing least-squares fitting of measured loss cones, in order to solve for parameters describing the vertical neutral atmospheric mass density profile from 160 to 230 km. Results are presented of mass densities in the southern hemisphere at 2 a.m. LST at the mean altitude of greatest sensitivity, 180 km, continuously over four martian years. Seasonal variability in densities is largely explained by orbital and latitudinal changes in dayside insolation that impacts the nightside through the resulting thermospheric circulation. However, the physical processes behind repeatable rapid, late autumnal cooling at mid-latitudes and near-aphelion warming at equatorial latitudes is not fully clear. Southern winter polar warming is generally weak or nonexistent over several Mars years, in basic agreement with MGS and MRO accelerometer observations. The puzzling response of mid-latitude densities from 160° to 200° E to the 2001 global dust storm suggests unanticipated localized nightside upper thermospheric lateral and vertical circulation patterns may accompany such storms. The downturn of the 11-year cycle of solar EUV flux is likely responsible for lower aphelion densities in 2004 and 2006 (Mars years 27 and 28).
© 2007 Elsevier Inc. All rights reserved.

Keywords: Mars; Magnetic fields; Mars, atmosphere

1. Introduction

Excepting two species-specific atmospheric density profiles provided by the Viking Landers (Nier and McElroy, 1977), most of our knowledge of the structure and dynamics of the martian thermosphere has come from accelerometer measurements of atmospheric drag, taken during the aerobraking phases of the Mars Global Surveyor (MGS) (09/1997–03/1998, 09/1998–02/1999) and Mars Odyssey (ODY) (10/2001–01/2002) missions. The Mars Reconnaissance Orbiter (MRO) spacecraft recently completed aerobraking (03/2006–08/2006), though no associated refereed publications yet exist. Mars Express (MEX) SPICAM nightglow (NO*) measurements also serve to constrain the Mars thermospheric circulation and variations with the Mars seasons (Bertaux et al., 2005).

From these measurements, significant discoveries have been made about general atmospheric structure (Keating et al., 1998; Bougher et al., 1999a, 1999b), zonal density variations caused

* Corresponding author.
  E-mail address: rlillis@ssl.berkeley.edu (R.J. Lillis).

by thermal tides (Joshi et al., 2000; Forbes and Hagan, 2000; Forbes et al., 2002; Wilson, 2002; Withers, 2003; Withers et al., 2003; Bougher et al., 2004; Angelats i Coll et al., 2004), seasonally-dependent meridional density gradients (Withers, 2006) and global circulation patterns, including strong northern winter polar warming (Bougher et al., 2006). These discoveries have served as invaluable input for models of global upper atmospheric circulation (Bougher et al., 1990, 1999a, 1999b, 2000, 2002, 2004; Angelats i Coll et al., 2005), which continue to evolve, both as the physical basis for understanding observations and for directing safe, fuel-efficient spacecraft aerobraking operations. However, the sampling is not nearly complete with respect to season, solar activity, latitude and local time and the measurements have been limited in altitude by accelerometer sensitivity and fuel tank sloshing, with MGS and ODY obtaining densities from ∼100 km (i.e. approximate periapsis altitude) up to 160 km (Withers, 2006) and MRO up to 170 km (Keating et al., 2006).

The atmospheric neutral density profile (i.e. density as a function of altitude) is a key factor in determining the details of loss cone formation in near-Mars space, i.e. the pitch angle-dependent attenuation of magnetically reflected solar wind electron fluxes traveling upward from Mars, as frequently observed by the MGS MAG/ER experiment (Mitchell et al., 2001; Lillis et al., 2004, 2008a). An atmospheric profile must be assumed *a priori* in order to use measured loss cones to perform electron reflection (ER) magnetometry, a technique to remotely infer magnetic field magnitudes at the surface of electron absorption, generally much closer to the magnetized crustal rocks than is possible with an *in situ* magnetometer (Lin, 1979; Acuña et al., 1992; Lillis et al., 2004, 2008b; Mitchell et al., 2007). However, in regions of Mars where crustal magnetic fields are strong enough, and well-sampled enough by low-altitude magnetometer data, to be confidently approximated by spherical harmonic expansions (Cain et al., 2003), this technique can be used 'in reverse' to solve for parameters describing the atmospheric neutral density profile. This technique was outlined, and some preliminary results presented, by Lillis et al. (2005). However, many details were omitted, important aspects of the technique have since been improved and there now exist an additional 21 months of data. In this paper we present, in fuller detail, the technique of ER density probing, as well as results showing variations in neutral mass densities in the southern hemisphere, at 2 a.m. local time and 180 km altitude, continuously over four full martian years (7.5 Earth years), from April 1999 to October 2006. Though the ER instrument was not designed for this purpose and the uncertainties are large for a single measurement, we will show that long-term trends in densities can be extracted through averaging over timescales of weeks to months.

2. Method

2.1. Loss cone model

Lillis et al. (2008a) describe in detail the theory of electron reflectometry in a planetary atmosphere, presenting a kinetic model of electron transport along open magnetic field lines [i.e. those connected to both the planetary crust and interplanetary magnetic field (IMF)], through an extended atmosphere, which predicts the shapes of loss cone pitch angle distributions at MGS mapping altitudes of ∼400 km. Parameters in this model which describe electrostatic potentials, magnetic field magnitude and atmospheric neutral density profiles between ∼400 km and the electron absorption region at ∼160–240 km, may be constrained by least-squares fitting to loss cones measured by MAG/ER (for examples, see Figs. 10 and 12 of Lillis et al., 2008a).

Our intent is now to show how this model can be used to least-squares fit the measured loss cones in order to solve for parameters describing the atmospheric neutral density profile in regions of Mars where the magnetic profile can be confidently assumed *a priori*. Due to the number of variables (3) we shall use to parameterize the atmospheric profile, we will be unable to simultaneously constrain electrostatic potentials. In Lillis et al. (2008b), these electrostatic potentials, parameterized by constant magnetic field-aligned electric fields, are solved for and are found to have a dependence on geographic location, being stronger in magnetic cusp regions, in which a transition is observed from open to closed magnetic topologies (e.g., Brain et al., 2003). We shall account for this effect by applying a separate post-correction to derived mass densities in each $1° × 1°$ box used in this study, as discussed later.

2.2. Choosing the magnetic field profile

As input to the model, we require an assumed magnetic field magnitude $B(x)$ where x is the distance tangential to the field line. But we also require $B(h)$ or $x(h)$ because the neutral density is expressed as a function of altitude h above the datum and the field line is never precisely vertical (i.e. its elevation angle is not 90°) nor straight (i.e. it is curved). Thus the most convenient form for the magnetic profile is three isomorphic arrays: x, h, B as shown in Fig. 1. We now must choose a magnetic field model and pick out the regions where we can trust this model to be a reliable representation of the true magnetic profile.

2.2.1. Choosing a martian global magnetic field model
There have been several attempts to develop an accurate three-dimensional global model of the vector magnetic field in the near vicinity of Mars based upon various combinations of magnetometer measurements from the aerobraking, science phasing and mapping segments of the MGS mission, with differing weighting of mission segments and field components. Purucker et al. (2000) and Langlais et al. (2004) modeled the source of the magnetic field as >10,000 separate dipoles in the crust, whereas Whaler and Purucker (2005) modeled the source as a spatially continuous distribution of magnetization, minimizing the total RMS magnetization in the entire crust. In both these approaches, the three-dimensional magnetic field $\boldsymbol{B}$ is calculated as minus the gradient of a magnetic vector potential $\boldsymbol{V}$, which must first be calculated from the modeled crustal magnetization $\boldsymbol{M}$.
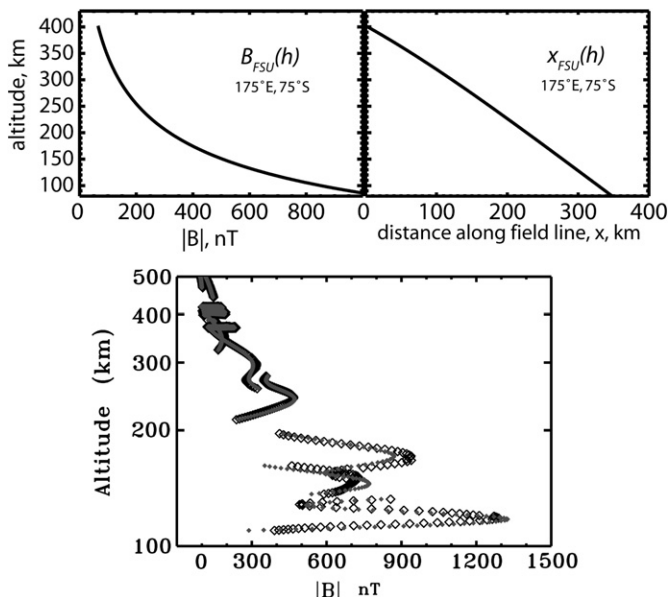
Fig. 1. Top panels: sample FSU model isomorphic arrays *B*, *h*, *x* that are necessary for a loss cone calculation. The magnetic profile $B_{\text{FSU}}(h)$ and the electron's distance traveled along the field line $x_{\text{FSU}}(h)$ are plotted versus altitude for the 1° × 1° box centered at 175° E, 75° S. Bottom panel: Cain et al. (2003) model predictions (unfilled black diamonds) vs magnetometer measurements (filled small gray diamonds) at a range of altitudes in a 10° × 10° box from 50° to 60° S and 170° to 180° E.

For the purposes of solving for neutral densities, we are interested only in the magnetic profile along the field line. The subsurface magnetization is unimportant, so we choose instead the model of Cain et al. (2003) (hereafter called 'FSU' for Florida State University), which is calculated by using magnetometer measurements to directly determine a spherical harmonic expression for the magnetic potential *V*, expressed as a linear expansion of normalized associated Legendre–Schmidt functions up to degree and order 90. This is preferred over the degree and order 50 model of Arkani-Hamed (2001, 2002) because its higher order allows it to better capture the details of the total magnetic field (i.e. internal plus external), in which we are interested for our purposes.

2.2.2. Geographic regions of model validity

As discussed in Section 7 of Lillis et al. (2008a), changes in the magnetic profile due to variability in the magnetotail field are far less important for loss cone shape prediction in regions where the crustal magnetic fields are strong compared to weak. For this reason, we choose only regions where the magnitude of the radial component of the model crustal magnetic field is higher than 50 nT at 400 km, approximately five times greater than the average non-crustal field on the nightside. We choose the radial component because radial crustal magnetic fields are more likely than tangential fields to connect with the sunward/anti-sunward magnetotail field due to their similar orientation. The crustal field in these regions displays a power law dependence on altitude (with an average exponent of ~2.2; Brain et al., 2003), reaching magnitudes of up to 900 nT at 180 km, while in comparison the magnetotail field is usually less than 15 nT, does not change with altitude and thus

contributes negligibly to the total field. This geographical constraint results in ~1600 1° × 1° boxes or approximately 2.5% coverage of the planet.

We only wish to analyze loss cones in geographic regions where the magnetic field lines at spacecraft altitudes (~400 km) intersect with the exobase (defined as the altitude at which a neutral atom's mean free path is equal to the atmospheric scale height; below the exobase lies the collisional atmosphere). Because the crustal magnetization morphology is complex and inhomogeneous and because the FSU model is semi-empirical, there are a significant number of cases where the radial field at the spacecraft is greater than 50 nT but the magnetic field lines, when traced downwards, turn around and head back upwards before turning downwards once more and reaching the exobase. We exclude these pathological cases even if the field lines eventually intersect the exobase because here we are less certain of the accuracy of the field line tracing, because the strong curvature effects could violate the adiabaticity of the electrons' motion and because we wish to keep the analysis as simple as possible. This filtering of pathological cases reduces our geographical coverage to ~1200 1° × 1° boxes or approximately 1.6% of the planet's surface. The remaining valid regions are shown in Fig. 2, entirely in the southern hemisphere and mostly between 160° and 200° E, with a small patch around 40° E.

2.3. Parameterization of the neutral density profile

The two main constituents in the martian upper thermosphere are carbon dioxide (CO_2) and atomic oxygen (O) (Nier and McElroy, 1977). Above the homopause (~100–120 km), the two species are not well-mixed and so have different scale heights based upon their relative molecular masses (44 and 16 atomic mass units, respectively) and temperatures. For simplicity, we parameterize a 2-species isothermal atmosphere and express the density as a function of altitude, correctly accounting for the variation in the acceleration due to gravity, as follows:

$$n_i(h) = n_{0i} \exp\left[-\int_{h_0}^{h} \frac{dh'}{H_i(h')} \right],$$

$$H_i(h) = \frac{kT(R_{\text{Mars}} + h)^2}{m_i G M_{\text{Mars}}}, \tag{1}$$

where h_0 is a reference altitude (we choose 160 km because this is a likely minimum altitude of sensitivity for cases of strong crustal magnetic field, as shown in the middle right panel of Fig. 15 in Lillis et al., 2008a), *i* is the species index, n_{0i} is the number density at h_0, $H_i(h)$ is the altitude-dependent scale height, *T* is the constant temperature above h_0 (a good approximation; Bougher et al., 2002), *k* is the Boltzmann constant, *G* is the universal gravitational constant, m_i is the mass of a molecule of species *i* and R_{Mars}, M_{Mars} are the radius and mass of Mars, respectively. $n_{0\text{-}CO_2}$, $n_{0\text{-}O_1}$ and *T* are the free parameters which we may adjust to fit the observed loss cone. The altitude *h* that we consider is the altitude above the areoid in the same 1° × 1° bins (i.e. the martian equivalent of the geoid, the surface of constant gravitational potential with an average radius
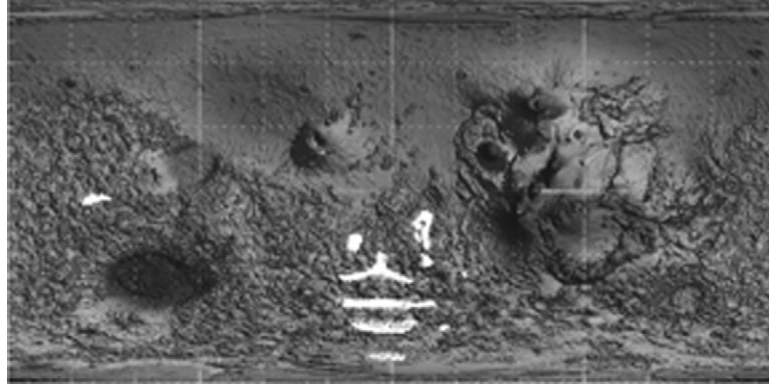
Fig. 2. Shown in white are the geographic regions of Mars where crustal magnetic field lines are consistently open and the radial component of the magnetic field is >50 nT, overlaid on shaded MOLA topography (Smith et al., 2001).

equal to that of the solid planet; Smith et al., 2001) because atmospheres respond to gravitational potential, not altitude above the solid surface (which can be highly nonuniform). Attempting to model the atmospheric density profile with more than three parameters is computationally prohibitive and given the relatively small effect of the neutral density profile on the loss cone shape (Lillis et al., 2008a) and the 22.5° angular resolution of the instrument (Mitchell et al., 2001), fitting the data to a more sophisticated atmospheric model would likely be unnecessary even if it were feasible.

2.4. Inferring neutral densities

Rather than calculate all the loss cones necessary to fit for $n_{0\text{-}CO_2}$, $n_{0\text{-}O_1}$ and T separately each time for each observed loss cone, it is faster and more convenient to pre-calculate all possible loss cone shapes for all combinations of parameters that we are likely to encounter in the data and place them in a 'look-up library' for easy comparison to the $\sim 3 \times 10^5$ observed loss cones in the appropriate regions in the data set. Thus, using the loss cone model (i.e. Eq. (18) of Lillis et al., 2008a) with Eq. (1) as input for the density profile, we calculated model loss cone shapes for each of the ~ 1200 appropriate $1° \times 1°$ geographic pixels, in the 116, 191, 313 eV channels, for a range of 3087 possible atmospheres, parameterized by all combinations of 21 logarithmically-spaced values of $n_{0\text{-}CO_2}$ (5×10^6–5×10^{10} cm^{-3}), 21 values of $n_{0\text{-}O_1}$ (5×10^6–5×10^{10} cm^{-3}) and 7 linearly spaced values of T (140–200 K). These bounding values were chosen to bracket the physically reasonable predictions of the MTGCM (Bougher et al., 1999b).

We compare the measured values of P_{surv} (corrected for the effects of atmospheric backscatter, as discussed in Section 5 of Lillis et al., 2008a) to the pre-calculated model values of P_{surv} for every combination of $n_{0\text{-}CO_2}$, $n_{0\text{-}O_1}$, T in our search grid and calculate the goodness-of-fit χ^2, convolving appropriately from the 50 model pitch angle bins to the 8 overlapping instrumental pitch angle bins. Also, we only consider measured values of P_{surv} between 0.07 and 0.79 to minimize errors (Lillis et al., 2008a) and do not consider parallel electric fields in the

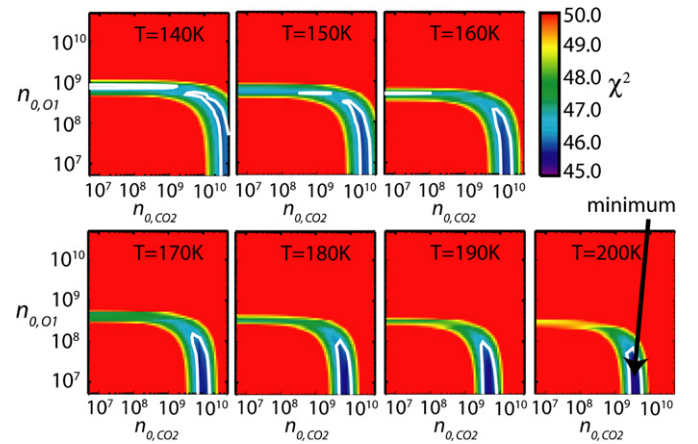Fig. 3. Complete 3-parameter χ^2 space for an example fit to a loss cone. The X and Y axes are number densities of CO_2 and O, respectively. Each panel shows a 'slice' in χ^2 space, corresponding to a single temperature from 140 to 200 K. Raw χ^2 values are shown to highlight the position of the 1-σ error hyper-ellipsoid, shown as a white line, which is defined as the space between $\min(\chi^2)$ and $\min(\chi^2) + 1.0$. The shape of this ellipsoid is typical and shows that T is very difficult to constrain and that it is almost impossible to isolate the contributions of CO_2 and O independently: only the total mass density is constrained.

fit because to do so would be computationally prohibitive. The correction for parallel electric fields is discussed in Section 3.4.

We find the values of $n_{0\text{-}CO_2}$, $n_{0\text{-}O_1}$, T which minimize χ^2. An example is shown in Fig. 3. This point in parameter space is our best fit and corresponds to an isothermal neutral density profile above 160 km. Due to instrumental uncertainties in the loss cone shape, $n_{0\text{-}CO_2}$, $n_{0\text{-}O}$ are almost entirely non-orthogonal parameters, i.e. they cannot be separately solved for and only their linear combination, comprising mass density, is constrained, as demonstrated by the shape of the error hyper-ellipsoids in Fig. 3. Because the much larger scale height of atomic oxygen gives a more gradual loss cone slope than CO_2, number densities of the two species could be separately extracted from measured loss cones if we had substantially better pitch angle resolution and a much higher instrumental geometric factor, beyond the capability of any current space physics instrumentation. Also shown in Fig. 3 is that the fitted values of T are almost completely unconstrained within the
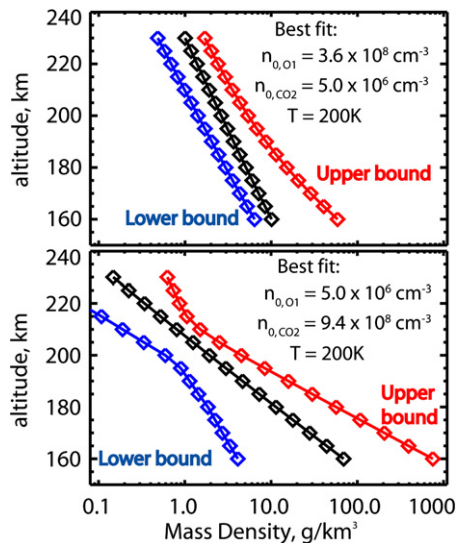
Fig. 4. Mass density profile and error envelope inferred for 2 example fits to observed loss cones. CO_2 is the dominant species in the bottom panel, whereas O dominates in the top panel. Their different molecular masses (44 and 16 atomic mass units) account for the large difference in scale heights (13.5 and 37 km, respectively). The best fit profiles intersect at ~180 km, which we will later determine to be the altitude of greatest sensitivity.

physically reasonable range probed. These properties of the fit are explained by the fact that the loss cone shape is sensitive to electron absorption over a very narrow range of altitudes, ~20–40 km (see Fig. 10). The low angular resolution of the ER instrument (22.5°) means there are typically only 1–3 flux measurements in the appropriate range where $0.07 < P_{surv} < 0.79$. Consequently, details of the vertical profile of electron absorption, and hence of atmospheric density, cannot be satisfactorily resolved. Thus we examine only mass density. The uncertainty in mass density at a given altitude is quantified by considering all points within the 1-σ error hyper-ellipsoid around the minimum of χ^2 and assigning upper and lower bound mass density values to be the highest/lowest mass density at that altitude as calculated using the values of $n_{0\text{-}CO_2}$, $n_{0\text{-}O_1}$, T in that ellipsoid in Eq. (1). This results in a best-fit mass density profile with an error envelope, as shown with examples in Fig. 4.

This method could be used in principle to 'solve' for densities at any altitude we wish because our three parameters uniquely define an entire atmospheric profile from the surface to the spacecraft. Of course these numbers are only meaningful within the range of altitudes over which the loss cone is formed which, given reasonable assumptions about the range of atmospheres we are likely to encounter, is approximately 160–230 km (Lillis et al., 2008a). In Section 3 we shall compare our inferred densities at these altitudes with the MTGCM atmospheres to check the validity of this assumption.

3. Data processing and results

The previous study of Lillis et al. (2005) on this topic only considered loss cones observed when MGS, at ~400 km altitude, was in the shadow of Mars, where the solar zenith angle (SZA) is >118°. In this study, we shall consider all loss cones

measured in the night hemisphere, including the region formerly excluded with solar zenith angles (SZA) between 90° and 118°. The reason is fourfold: (1) loss cones form much more frequently in this region than they do on the martian dayside, though not as frequently as in the deep shadow, ensuring reasonably good statistics; (2) photoelectrons produced when the upper atmosphere is in sunlight have energies generally below 60 eV (Fox and Dalgarno, 1979; Liemohn et al., 2006) and so should not contaminate the loss cones in the 90–400 eV range; (3) soft X-ray-produced oxygen Auger electrons, with energies near 500 eV, have substantially lower fluxes than magnetosheath or magnetotail electrons of the same energy (Mitchell et al., 2000) and hence should also not contaminate our measurements; and (4) while this region has additional magnetic turbulence in the induced external field, the magnetic gradients caused by this turbulence are negligible compared to the gradients of the strong crustal fields in the regions we analyze.

3.1. Discarding unreliable data

Fitting, in the manner described in Section 2.4, all clearly identifiable night side loss cones from the appropriate strong crustal field regions from April 1999 to October 2006 yields ~174,000 inferred mass density profiles. However, many of these profiles are unreliable for one or more of the three following separate reasons and must be discarded:

(1) *Magnetometer—FSU model disagreement*. We stipulate that the measured magnetic field associated with every pitch angle distribution must agree with the FSU model field at the spacecraft to within 5% in magnitude and 10° in direction. This eliminates 68.5% of the profiles, or ~119,000 measurements.
(2) *Poor fit to the loss cone*. The reduced value of the goodness-of-fit χ^2 must be less than 2.0 to eliminate cases where the model cannot fit the loss cone shape adequately well. This eliminates a further ~5000 measurements.
(3) *Unconstrained inferred densities*. We exclude any measurement where the loss cone shape does not permit us to bound the density within the very wide physically reasonable ranges of $n_{0\text{-}CO_2}$ and $n_{0\text{-}O_1}$ that were chosen for the parameter search. Fig. 5 demonstrates how to apply this in practice: we exclude measurements where the lower bound is equal to the lowest density possible in our parameter space or where the upper bound is equal or close to the highest density possible. This eliminates a further ~24,000 measurements.

After filtering this unreliable data, we are left with ~29,000 valid inferred density profiles, which we presently examine.

3.2. Seasonal latitude coverage

Field lines in the magnetic pileup region on the dayside and near the poles tend to be aligned with the local horizontal and unconnected to the crust whereas in the magnetotail on the night side, field lines at ~400 km are more likely to be vertical and
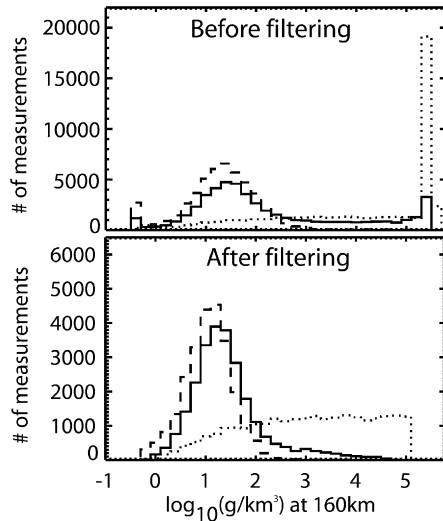
Fig. 5. Histograms demonstrating the filtering out of unconstrained inferred mass densities. The top panel is a histogram of the entire data set minus the poor fits and the points of magnetometer-FSU model disagreement. The dashed, dotted and solid lines represent the lower bounds, upper bounds and best fits, respectively. Approximately 3000 measurements are unconstrained at the lower bound and ~21,000 are unconstrained at the upper bound. The bottom panel shows the same histogram but with these unreliable measurements removed.
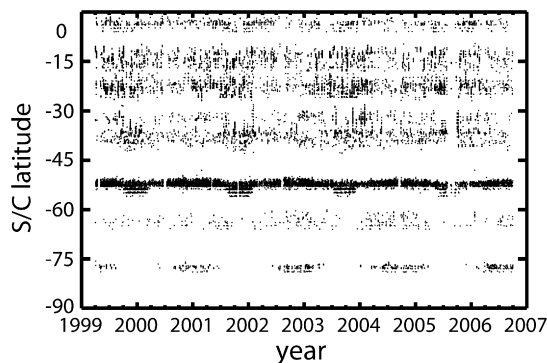

Fig. 6. Latitudinal distribution of ~29,000 inferred density measurements over 7½ years from 1999 to 2006. Each dot represents a single measurement.

open (Brain et al., 2003). Mars' obliquity of ~25° causes solar zenith angles at the same geographic location and local solar time (in which the spacecraft orbit is fixed, at 2 a.m.) to vary by up to 50° with season. Thus we observe an annual dependence (i.e. ~22.5-month cycle) in loss cone formation and hence data coverage for inferred mass densities poleward of 60° S. Fig. 6 illustrates this point. The non-uniform coverage north of 60° S is due to telemetry/data rates which vary on a 26-month cycle with Earth–Mars distance.

3.3. Error analysis

Errors in the remaining reliable inferred mass density profiles are both systematic and statistical. It is very difficult to quantify the systematic error in our inferred densities due to our chosen best-guess parameterization of the atmosphere. However, we can address the systematic error due to errors in the
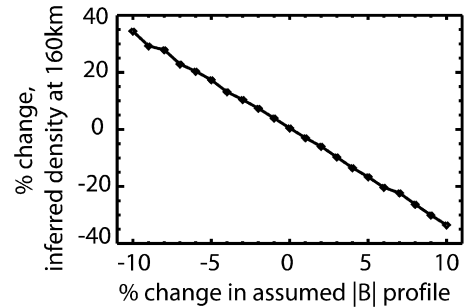

Fig. 7. Linear dependence of systematic inferred density errors upon errors in the assumed magnetic profile. Each density error value shown is the mean of ~200 simulation density fits in regions where the radial component of the crustal magnetic field is >50 nT. The noise is due to the inherent granularity of the fitting process.

assumed magnetic field profile. We shall then look at the statistical errors due to instrument limitations.

As mentioned above, we require better than 5% agreement between the FSU model and magnetometer measurements at the spacecraft mapping altitude of ~400 km. At lower altitudes, Cain et al. (2003) estimate errors of up to 20 nT between 110 and 170 km. At electron absorption altitudes (above 160 km), this represents a 4% to 10% error in field magnitude.

To quantify the resulting error in inferred densities, we performed simulation fits to hundreds of sample loss cones, artificially increasing/decreasing by 0–10% the magnetic field magnitude over the entire magnetic profile. The averaged results are shown in Fig. 7 and demonstrate that the density errors show a linear dependence upon the error in the assumed magnetic profile over the applicable range, with the relative uncertainty in density approximately equal to four times the relative uncertainty in the magnetic profile. Therefore, the worst-case systematic error in derived densities from 160 to 230 km, attributable to errors in the magnetic profile, is approximately 35%.

The propagated error envelopes shown in Fig. 5 demonstrate that there is natural statistical scatter in the data due to the instrument's limited ability to characterize the loss cone shape. Given the large uncertainties in a single measurement, our strategy is to group together the best-fit measurements in 84-day moving averages and thus attempt to extract long-term variations in upper thermospheric densities. This results in distributions like the example shown in Fig. 8. They have an approximately Gaussian shape with a strong peak and a more prominent tail at the upper end compared with the lower end. At each altitude, the standard deviations of these distributions are very close to the average difference between the lower bound and upper bound densities derived from the hyper-ellipsoids for each measurement, as expected. We deal with logarithms of density because the number densities were distributed logarithmically in parameter space for the fitting. Rather than simply taking the mean, which would be biased by this upper tail, we least-squares fit a simple Gaussian curve to each density distribution and thus determine its central value and standard deviation, as shown in Fig. 8, where the x-axis is $\log_{10}(\rho$ in g/km$^3)$. The standard error in the mean logarithm of the density, $\Delta(\log \rho)$, is given by the standard devi-
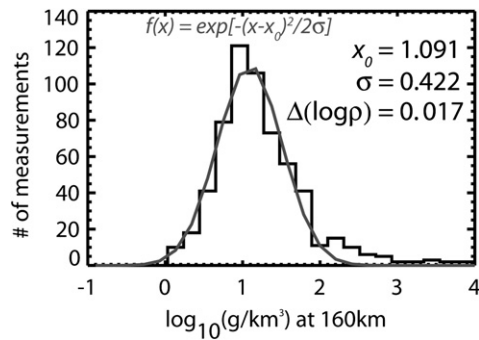
Fig. 8. Example histogram of all inferred mass densities from 45° to 60° S at 2:00 a.m. during March and April 2001. The mean and standard deviation of distributions are calculated by fitting a simple Gaussian curve (shown in gray) to the histogram. x is $\log_{10}(\rho$ in $g/km^3)$ and x_0 is the best fit value of x for the Gaussian peak.

ation σ divided by the square root of the number of measurements.

Another estimate of the statistical density error comes from the uncertainty in the fitting parameter x_0 (i.e. see Fig. 8), which turns out in most cases to be very close to the standard error mentioned above. It does not significantly depend upon the bin size chosen for the fitted histogram. These statistical errors in the logarithm of the density are, in 95% of cases <0.05 which is equivalent to <11% in density between 160 and 230 km.

3.4. Electric field correction

As mentioned in Section 2.1, simultaneously solving for our three density profile parameters plus the average magnetic field-aligned or 'parallel' electric field between the spacecraft and absorption region (i.e. ~150 to ~400 km) is computationally prohibitive. Instead, we apply a correction *a posteriori* to the reliable derived densities to account for this effect.

A radially positive electric field (i.e. radially outward from the planet) lowers the reflection altitudes of all precipitating electrons, raising their scattering probability and shifting the loss cone closer to 90° (e.g., Figs. 6, 12 of Lillis et al., 2008a). This effect is mimicked by a denser atmosphere, so that if such a field is present but not accounted for, the fitting procedure will obtain an artificially high value for atmospheric density. The opposite is true for a radially negative electric field.

When performing crustal magnetic field mapping using loss cones (explained in detail in Lillis et al., 2008b), the parallel electric field and singly-parameterized crustal magnetic field magnitude are simultaneously calculated, assuming a species-specific mean reference model atmospheric neutral density profile (calculated by scaling an equinox, equatorial, solar moderate MTGCM atmosphere to match the mean mass density at 180 km calculated in this paper). However, since electric field effects on loss cone shape are strongly energy-dependent while the effects of changes in the neutral density and magnetic profiles the electrons follow can mimic each other and are energy-independent (Lillis et al., 2008a), these derived electric field values are not dependent upon this assumed atmospheric profile and can therefore be used to correct the densities derived
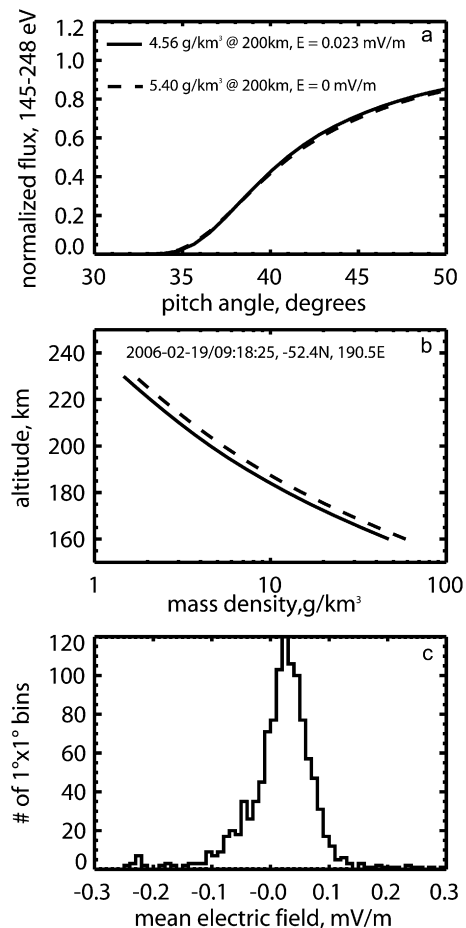

Fig. 9. (a) Two near-identical loss cones, one calculated with no electric field and the derived density profile from a loss cone measured at 2006-02-19/09:18:25 and location 52.4° S, 190.5° E (dashed line), the other calculated using the average measured electric field (from Lillis et al., 2008b) at that location and the 'corrected' density profile (solid line). (b) The corresponding fitted (dashed) and corrected (solid) mass density profiles. (c) Histogram of the average electric field in each of the ~1200 1° × 1° geographic bins used in this study.

from loss cone fitting (this paper) without resorting to circular reasoning.

For each reliable density measurement, an increase or decrease in density at all altitudes from 160 to 230 km is calculated for each of the three energy channels such that the loss cone shape with no electric field and the 'old' density is as close as possible (by least-squares fitting) to the loss cone shape with the measured electric field and the 'new' density. Figs. 9a and 9b show an example of this. We then take the average of the new density calculated from the three channels as our 'corrected' density. It should be noted that this correction, while improving the accuracy of the derived densities overall, introduces an additional statistical error which we estimate to be typically <20%.

The electric field values used are mean values in each 1° × 1° bin averaged over all four martian years, and have considerably lower corresponding statistical scatter than using electric field values from individual loss cones due to the poor angular resolution of the ER instrument. A histogram of these electric field values, by geographic location, is shown in Fig. 9c.
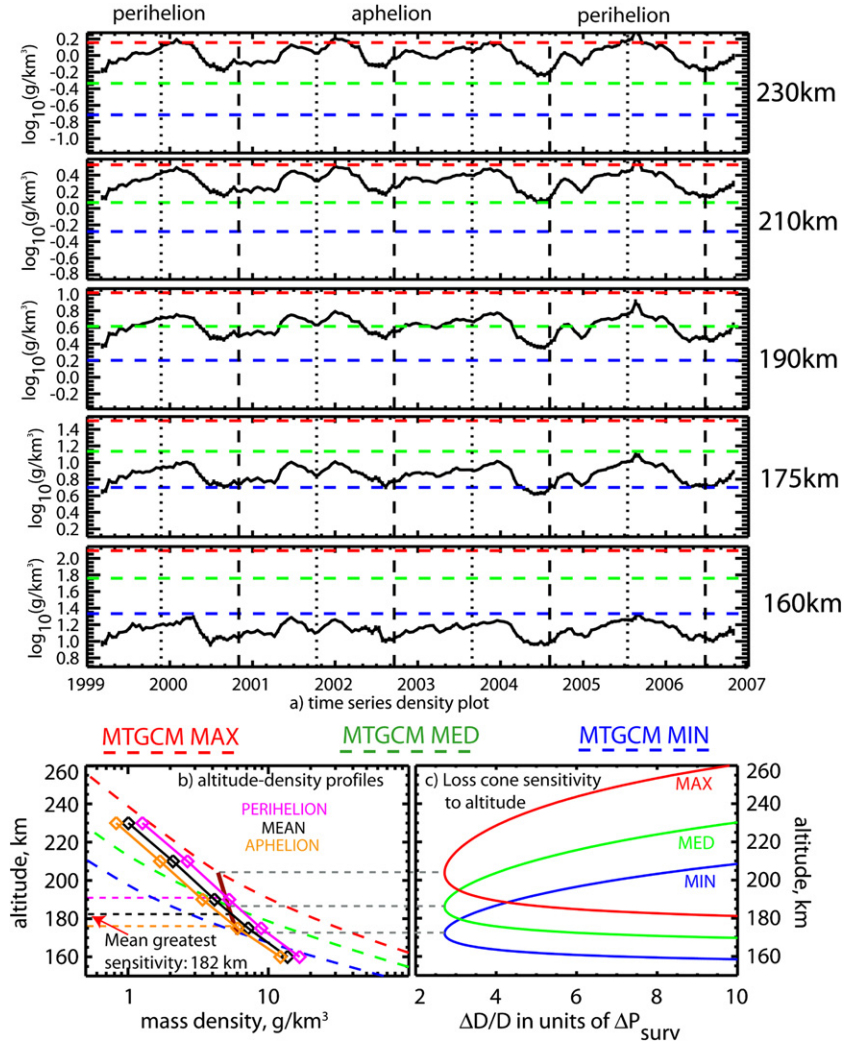
Fig. 10. Three equatorial 2:00 a.m. MTGCM model atmospheres (MAX, red: solar maximum, perihelion; MED, green: solar moderate, equinox; MIN, blue: solar minimum, aphelion) are compared with (a) time series plots of all data in 2-month bins at five sample altitudes and (b) altitude–density profiles for time-averaged mean conditions (black) and conditions within 60 days of Mars' aphelion (orange) and perihelion (purple). Panel (c) plots the fractional error in scattering depth (see Section 7 of Lillis et al., 2008a) as a function of altitude for the same magnetic profile shown in Fig. 1 and for the three model atmospheres. The horizontal dotted lines connecting panels (b) and (c) represent the altitudes of greatest sensitivity (i.e. smallest fractional error) for the model profiles, densities at which are joined by the short brown line in panel (b). We estimate our altitudes of greatest sensitivity [shown by horizontal black, orange and purple dotted lines in panel (b)] by the intersection between these densities and the inferred density profiles. (For interpretation of the references to color in this figure legend, the reader is referred to the web version of this article.)

3.5. Data overview and altitude dependence

Before we can analyze or interpret the inferred densities, we must examine the overall character of the data and ensure that the loss cones are sensitive to density variations at the altitudes we choose. Fig. 10a gives an overview of the densities at several altitudes, showing that the densities at all probed altitudes display regular variation with each martian year around a mean with maximum/minimum densities occurring near perihelion/aphelion, respectively, also corresponding with summer/winter in the southern hemisphere, where all data is collected.

Fig. 10 also demonstrates that for a typical strong crustal field region, loss cones are sensitive (i.e. the fractional error in dimensionless scattering depth, $\Delta D/D$ is less than twice its minimum value, as discussed in Lillis et al., 2008a) to the range

of altitudes where the mass density and increases from ~1.5 to ~20 g/km^3, which according to our inferred densities, is approximately 160–230 km. It further demonstrates that, under these strong crustal magnetic conditions, loss cones are maximally sensitive to the altitude where mass density is ~4.5 to 6.5 g/km^3.

We estimate this altitude of greatest sensitivity to be that at which the inferred density profile intersects the line joining the altitudes and densities of greatest sensitivity for the 3 model cases (shown by the brown line in Fig. 10b). This turns out to be 176, 182 and 191 km for the aphelion data, overall mean data and perihelion data, respectively. Since meaningful comparisons between densities can only be made at a common altitude, we choose 180 km for these comparisons and are unconcerned about the small differences in sensitivity between these nearby altitudes.
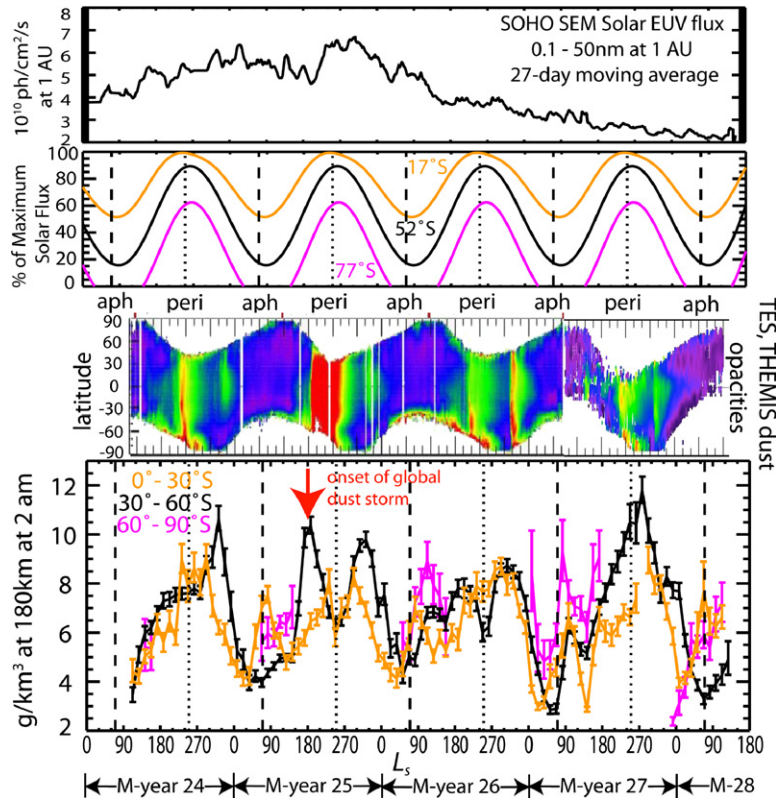
Fig. 11. The bottom panel plots 84-day moving averages of inferred density at 180 km at 2:00 a.m. as a function of Mars' solar longitude (L_s) in the following latitude ranges: 0°–30° S (orange), 30°–60° S (black) and 60°–90° S (purple) over four complete martian years. Error bars are standard errors as discussed in Section 3.3. The lower middle panel plots TES and THEMIS derived dayside IR dust opacities as a function of time and latitude (M. Smith, personal communication). Purple represents a dust optical depth of 0, while red represents 0.5. The upper middle panel plots peak daytime solar flux, as a percentage of the maximum flux striking Mars, at median latitudes of density measurements in the 3 latitude ranges: 17° S, 52° S, 77° S. Vertical dotted/dashed lines represent Mars perihelion/aphelion, respectively. The top panel plots 27-day moving averages of solar EUV flux extrapolated to 1 AU from SOHO SEM, with the impulsive and decay phases of all flares manually removed. For reference, Mars year 1 (or M-year 1) began at date/time: 1955-04-11/06:29:16. (For interpretation of the references to color in this figure legend, the reader is referred to the web version of this article.)

3.6. Temporal binning

With a significant statistical scatter amongst individual data points, temporal and latitudinal bins must be chosen wide enough to ensure enough measurements in each bin to adequately estimate the center of the Gaussian curve that we fit to the distribution (Fig. 8). Upon inspection of individual distributions, a minimum of 40 measurements appears sufficient. Thus, to ensure comparability between latitude bins, we express density time series as an 84-day moving average. This binning scheme allows continuous coverage over four martian years in the 0°–30° S and 30°–60° S latitude ranges, while the 60°–90° S range does not have sufficient sampling near perihelion, as shown in Fig. 11, bottom panel.

4. Analysis and interpretation of density variability

Variations in nighttime upper atmospheric densities can be divided into two main categories: seasonal and inter-annual. We shall examine these variations separately, along with their probable causes.

4.1. Seasonal variability

To first order, densities in the nighttime upper atmosphere appear to be determined by heating effects (and hence increased scale heights) caused by the flux of infrared, visible and ultraviolet solar radiation striking the dayside surface and the entire column of atmosphere (Bougher et al., 2000). In this first order approximation, the solar flux striking a square meter of the atmosphere over a day at a given latitude varies with the inverse square of Mars' heliocentric distance and with the cosine of the maximum solar zenith angle, as shown in the second panel of Fig. 11.

This seasonally variable insolation has an obvious effect on upper thermospheric densities, as shown in the bottom panel of Fig. 11, which shows 84-day moving averages of densities in three southern hemisphere latitude bands: equatorial (0°–30° S), mid-latitude (30°–60° S) and polar (60°–90° S). It can clearly be seen that the highest/lowest nightside densities generally occur near perihelion/aphelion when daytime solar radiation flux is at its seasonal maximum/minimum, respectively. This changing dayside heating drives a day-to-night thermospheric circulation that determines the nightside heating and

the seasonal variation of the temperature and density structure (e.g., Bougher et al., 2006; Bell et al., 2007).

Within this overall seasonal pattern, there are differences between latitudes as one would expect. First of all, the seasonal amplitude of densities is somewhat larger for the mid-latitude region (factor of 1.6–4.0) than for the equatorial region (factor of 1.5–2.5), presumably due to the larger seasonal change in the incident mid-latitude solar fluxes. Second, the southern autumnal density drop (i.e. from $L_s = 270°$–$20°$) at mid-latitudes lags $\sim$2 months behind that nearer the equator at the ends of M-years 24 and 25. (For reference, one Mars year is 686.98 Earth days and Mars year 1 (abbreviated as MY1 or M-year 1) began at date/time: 1955-04-11/06:29:16.) This could be partially due to the equatorial latitudes reaching their maximum insolation $\sim$2 months before the mid-latitudes but reaching their minimum simultaneously, as shown in the second panel of Fig. 11. In addition, the timing of maximum solar insolation at mid-latitudes in conjunction with the inter-annual variation of the timing of seasonal dust events (i.e. some events as early as $L_s = 180°$, others as late as $L_s = 330°$) may combine to provide a sharp density decline at the end of the dusty season (see Section 4.2). Third, equatorial densities display a repeatable $\sim$60–100% increase immediately around aphelion, lasting $\sim$5 months. Last, though data in the polar latitude band is sparse, aphelion polar densities are higher than mid-latitude (and sometimes equatorial) densities in some years but not others, though never lower. This suggests that southern winter polar warming is not a consistently repeating feature of the martian upper atmospheric circulation, unlike its northern counterpart (Bougher et al., 2006). In particular, little or no southern winter polar warming was seen during the most recent aphelion in June 2006, consistent with recent MGCM–MTGCM simulations (Bougher et al., 2006, 2007) and with accelerometer measurements from the MRO spacecraft, which was aerobraking with periapsis in the southern winter polar night at that time (Bougher and Keating, 2006; Keating et al., 2006).

4.2. Inter-annual variability

Inter-annual variations should be examined using low ($0°$–$30°$ S) and mid ($30°$–$60°$ S) latitude datasets where continuous coverage exists over the full 4 martian years. It is noteworthy that inter-annual density patterns do not exactly repeat from year to year. Causes for such inter-annual variability are either transient or are tied to the 11-year solar cycle. Examples of transient events are (a) space weather events, e.g. solar energetic particle (SEP) storms, solar X-ray flares or interplanetary coronal mass ejections (ICMEs), which happen on time scales (hours/days) too short to be observable with this data set and (b) lower atmospheric dust events, which vary considerably in their timing and intensity from one Mars year to the next (e.g., Liu et al., 2003; Smith, 2004).

4.2.1. Response to the 2001 global dust storm

There was one large, long-duration dust storm which occurred during this MGS/ER sampling time interval: the June–
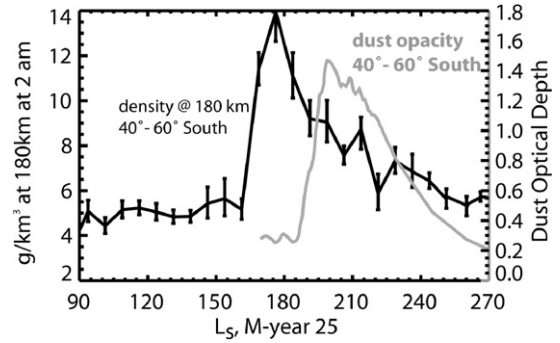

Fig. 12. Onset and decay of 2001 global dust storm. 14-day density averages (left axis, black line) and 1-day zonally-averaged TES dust opacities (right axis, gray line) are plotted as a function of Mars' solar longitude (L_s).

November 2001 global dust storm, which raised lower atmospheric temperatures by up to $50°$ K for several months (Smith et al., 2002). The storm's apparent effect on the nightside upper thermosphere is puzzling, as shown in Figs. 11 and 12. At a time when we might otherwise expect to see a steady rise in densities at all southern latitudes at or after the storm's onset, we see a sharp increase in densities at mid-latitudes only (from $160°$ to $200°$ E), coincident with some moderate dust activity at those latitudes (see Fig. 11) but $\sim$1 month before the main storm began. This is followed by a gradual decrease in density during the storm until just after perihelion, when the lower atmosphere had substantially cleared, after which the densities quickly rebounded to their seasonal norm.

Fig. 12 shows 14-day density averages from $160°$ to $200°$ E (e.g., see Fig. 2) and 1-day zonally-averaged dust opacities (M. Smith, personal communication) in the $40°$–$60°$ S latitude band (chosen due to pre-binning of the TES data), during a time interval encompassing the storm ($L_s = 90$–270). It highlights the rapid rise in mid-latitude densities $\sim$40 days before the onset of the storm, at a time when equatorial densities behaved unremarkably, rising as expected with increasing dayside insolation. Whatever the cause of this sharp increase, the near-simultaneous timing of the subsequent density decrease with the main phase of the storm, made even more remarkable in the context of the natural seasonal pattern of increasing densities, raises the possibility of a localized storm-induced downwelling in the upper atmosphere in this fairly small latitude and longitude range where our data exists ($40°$–$60°$ S, $160°$–$200°$ E). Interestingly this region was substantially less dusty than any other longitude range in the southern hemisphere during the first 30 days of the storm's onset (Fig. 1; Smith et al., 2002). When the lower atmosphere cleared, this putative downwelling may have ceased, allowing the rapid rebound of post-perihelion densities, consistent with seasonal pattern observed during other years (see Section 4.1).

The apparent anti-correlation of nightside mid-latitude densities with a global dust storm, coupled with the unremarkable behavior of the equatorial densities during the evolution of the same storm, implies that, although dust storm effects have

been linked to dayside density variations at 130 km (Keating et al., 1998; Bougher et al., 1999a), storm effects may not be easily linked to nightside density variations in the upper thermosphere.

4.2.2. Solar cycle effects

Solar extreme ultraviolet (EUV) flux varies regularly over the 11-year solar cycle, affecting upper thermospheric densities through direct heating and ionization (Bougher et al., 1999b, 2000). Fig. 11 also plots the solar EUV flux (0.1–50 nm) with flares removed manually (i.e. all measurements during flare spikes and their decay phases were removed), as measured by the SOHO SEM instrument, extrapolated to 1 AU and smoothed over 27 days to average out effects of the Sun's rotation. There is a broad maximum during M-year 25, then a nearly constant decline towards solar minimum in M-year 28. A possible effect of this decline is seen during the aphelion periods of M-year 27 and M-year 28, when the EUV flux is reduced by ~60% from its maximum and where the density minima appear to be 25–35% lower than in M-years 25 and 26. However, low EUV flux cannot by itself explain the fourfold increase in mid-latitude densities from the M-year 27 aphelion to the following perihelion.

4.3. Comparisons with thermosphere simulations

Despite limited geographic coverage, the continuous nature of the MGS ER data set makes it very useful in guiding the development of thermospheric global circulation models, the improvement of which is essential, both for understanding the complex dynamics which drive planetary atmospheres and for safe, confident spacecraft aerobraking maneuvers. Here we present some preliminary comparisons between this data and the coupled MGCM–MTGCM framework (defined below).

4.3.1. Brief review of MGCM–MTGCM coupling framework

The Mars Thermosphere General Circulation Model (MT-GCM) is a finite difference primitive equation model that self-consistently solves for time-dependent neutral temperatures, neutral–ion densities, and three component neutral winds over the globe (e.g., Bougher et al., 1999a, 1999b, 2000, 2002, 2004). Prognostic equations for the major neutral species (CO_2, CO, N_2, and O), selected minor neutral species [Ar, He, O_2, NO, N(4S)], and several photochemical ions (e.g., O_2^+, CO_2^+, O^+, and NO^+ below 180 km) are included. These fields are simulated on 33-pressure levels (above 1.32 microbar), corresponding to ~70–300 km (solar maximum conditions), with a $5° \times 5°$ latitude and longitude resolution. The vertical coordinate is log-pressure, with a vertical spacing of 0.5 scale heights. Key adjustable parameters which can be varied for individual MTGCM cases include the F10.7 or E10.7 index (solar EUV/FUV flux variation), heliocentric distance (orbital variation), and solar declination (seasonal variation). At present, a simple dayside photochemical ionosphere is formulated within the MTGCM (e.g., Bougher et al., 2004), based upon the key ion–neutral reactions and rates of Fox and Sung

(2001), and making use of empirical electron and ion temperatures adopted from the Viking mission. Recently completed upgrades for the MTGCM code include a fast Non-Local Thermodynamic Equilibrium (NLTE) 15-micron cooling scheme along with the corresponding near-IR heating rates (e.g., Lopez-Valverde et al., 1998; Lopez-Valverde, private communication).

The MTGCM is currently driven by the NASA Ames Mars General Circulation Model (MGCM) code (e.g., Haberle et al., 1999) at the 1.32-microbar level (near 60–80 km), permitting a detailed coupling across this boundary that captures both migrating and non-migrating upward propagating tides and the thermal expansion and contraction of the Mars lower atmosphere with the passage of the seasons and dust events (e.g., Bougher et al., 2004, 2006). Realistic latitudinal and vertical dust distributions are now being prescribed within the MGCM for various Mars seasonal conditions throughout the martian year (e.g., Bell et al., 2007). Key prognostic and diagnostic fields are passed (upward) from the MGCM to the MTGCM at the 1.32-microbar pressure surface at every MTGCM gridpoint. These two models are each run with a 2-min timestep, with the MGCM exchanging fields with the MTGCM at this frequency. Ten martian day simulations are typically conducted for various Mars seasonal and solar cycle conditions. Model histories are archived at 1-h intervals throughout the martian day to capture the impact of longitude forcing upon time-dependent (specific local time) features.

4.3.2. Comparisons of MGCM–MTGCM simulations with MGS/ER datasets

Specific MGCM–MTGCM simulations have been conducted appropriate to $L_s = 90$ and 270 conditions and MGS Thermal Emission Spectrometer (TES) mapping year dust opacities (from TES years #1 and 2, corresponding to MY 24–26). In addition, solar fluxes have been prescribed corresponding to spacecraft observational periods. Specifically, calculations were made for: (a) MGS Phase 2 aerobraking ($L_s \sim 90$, F10.7 $\sim$ 130, TES #1) in early 1999 (i.e. early MY 24), (b) conditions (no aerobraking) in early MY 25 ($L_s \sim 90$, F10.7 $\sim$ 130, TES #1), (c) ODY aerobraking ($L_s \sim 270$ and 300, F10.7 $\sim$ 175, TES #2) in early 2002 (i.e. late MY 25), and finally (d) conditions (no aerobraking) in early MY 26 ($L_s \sim 90$, F10.7 $\sim$ 150, TES #2). Simulated 2 AM densities spanning 160–200° E longitude at 180 km from these four cases are compared with corresponding MGS/ER densities obtained during overlapping sampling periods. MGCM–MTGCM calculations for periods after January 2004 require MGCM forcing using ODY THEMIS dust opacity datasets (not yet available for usage).

Data-model comparisons (not shown) reveal that both $L_s \sim$ 90 simulated and measured densities are nearly unchanged from 1999 to 2004, consistent with the behavior of the solar fluxes during this period. Furthermore, calculated density magnitudes are in general agreement with observations, and are also consistent with weak winter polar warming features (i.e. slightly enhanced densities toward the winter pole) during these aphe-

lion periods. This variable yet generally weak polar warming is consistent with previous MGCM–MTGCM aphelion calculations (e.g., Bougher et al., 2006; Bell et al., 2007). Near perihelion ($L_s \sim 270$–300) during early 2002 (after the dust storm abatement), simulated low-latitude densities match MGS/ER measured values of ~ 7–8 g/km^3. However, simulated densities rise by a factor of ~ 4–5 toward the continuously sunlit southern summer pole, while MGS/ER densities appear to increase more gradually to 10 g/km^3 at mid-latitudes. MGS/ER data needed to confirm this predicted summer polar density enhancement is missing poleward of 55° S.

5. Concluding remarks

In summary, by measuring the pitch angle distributions of magnetically reflecting solar wind electrons in regions of Mars where the magnetic field lines are open and the crustal magnetic field is sufficiently strong that it dominates the induced magnetotail field (mostly between 160° and 200° E), we can model the electrons' interaction with upper thermospheric neutrals and thus infer densities of those neutrals at ~ 180 km and their variation over long periods. This results in a continuous record of upper thermospheric densities from 0° to 60° S and near-aphelion densities from 60° to 90° S at 2 a.m. SLT over four complete martian years. This record displays a correlation with annual variations in insolation caused by Mars' axial tilt and eccentric orbit: densities are highest near perihelion and lowest near aphelion with a larger amplitude of variation and later autumnal cooling at mid-latitudes compared with equatorial latitudes. There is a puzzling anti-correlation between mid-latitude densities and the 2001 global dust storm, possibly suggesting a localized downwelling in the night side upper thermosphere during the storm. Southern winter polar warming appears weak or nonexistent, consistent with simulations and observations at lower altitudes. Finally, lower densities during the last two aphelion periods can likely be attributed to lower solar EUV fluxes associated with the declining phase of the 11-year solar cycle.

Comparisons between these results and aerobraking accelerometer data would be helpful for 'ground-truthing' these results and for scientific studies. However, direct comparisons have not been thus far possible because MGS aerobraking finished in February 1999, shortly before the first ER measurements shown here. MGS ACC measurements in early 1999 were obtained between 90° and 30° S at 2 a.m. LST, but only extend up to 130 km. ODY aerobraking spanned October 2001–January 2002, but was restricted to the northern hemisphere. MRO aerobraking between March and September 2006 sampled the entire southern hemisphere, with many nightside periapses. This accelerometer data is expected to be archived in 2007. Comparisons to atmospheric profiles obtained by SPICAM stellar occultations will also be valuable. Ongoing analysis of orbiter radio tracking data has determined global-averaged atmospheric mass densities at 250 (ODY) and 400 (MGS) km altitude (Mazarico et al., 2007).

References

Acuña, M.H., and 16 colleagues, 1992. The Mars Observer magnetic fields investigation. J. Geophys. Res. Planets 97, 7799–7814.

Angelats i Coll, M., Forget, F., Lopez-Valverde, M.A., Read, P.L., Lewis, S.R., 2004. Upper atmosphere of Mars up to 120 km: Mars Global Surveyor accelerometer data analysis with the LMD general circulation model. J. Geophys. Res. 109, doi:10.1029/2003JE002163. E01011.

Angelats i Coll, M., Forget, F., Lopez-Valverde, M.A., Gonzalez-Galindo, F., 2005. The first Mars thermospheric general circulation model: The martian atmosphere from the ground to 240 km. Geophys. Res. Lett. 32, doi:10.1029/2004GL021368. L04201.

Arkani-Hamed, J., 2001. A 50-degree spherical harmonic model of the magnetic field of Mars. J. Geophys. Res. 106, 23197–23208.

Arkani-Hamed, J., 2002. An improved 50-degree spherical harmonic model of the magnetic field of Mars derived from both high-altitude and low-altitude datasets. J. Geophys. Res. 107 (E10), doi:10.1029/2001JE001835. 5083.

Bell, J.M., Bougher, S.W., Murphy, J.R., 2007. Vertical dust mixing and the inter-annual variations in the Mars thermosphere. J. Geophys. Res. 112 (E12), doi:10.1029/2006JE002856. E12002.

Bertaux, J.L., and 10 colleagues, 2005. Night glow in the upper atmosphere of Mars and implications for atmospheric transport. Science 307, 566–569.

Bougher, S.W., Keating, G.M., 2006. Mars Reconnaissance Orbiter: Aerobraking science analysis. Bull. Am. Astron. Soc. 38 (3), 605. Abstract 61.12.

Bougher, S.W., Roble, R.G., Ridley, E.C., Dickinson, R.E., 1990. The Mars thermosphere. II. General circulation with coupled dynamics and composition. J. Geophys. Res. 95, 14811–14827.

Bougher, S.W., Keating, G.M., Zurek, R.W., Murphy, J., Haberle, R., Hollingsworth, J., Clancy, R.T., 1999a. Mars Global Surveyor aerobraking: Atmospheric trends and model interpretation. Adv. Space Res. 23, 1887–1897.

Bougher, S.W., Engle, S., Roble, R.G., Foster, B., 1999b. Comparative terrestrial planet thermospheres. 2. Solar cycle variation of global structure and winds at equinox. J. Geophys. Res. 104, 16591–16611.

Bougher, S.W., Engle, S., Roble, R.G., Foster, B., 2000. Comparative terrestrial planet thermospheres. 3. Solar cycle variation of global structure and winds solstices. J. Geophys. Res. 105 (E7), 17669–17692.

Bougher, S.W., Roble, R.G., Fuller-Rowell, T.J., 2002. Simulations of the upper atmospheres of the terrestrial planets. In: Mendillo, M., Nagy, A., Waite, J.H. (Eds.), Atmospheres in the Solar System: Comparative Aeronomy. In: Geophysical Monographs, vol. 130. American Geophysical Union, Washington, DC, pp. 261–288.

Bougher, S.W., Engel, S., Hinson, D.P., Murphy, J.R., 2004. MGS Radio Science electron density profiles: Inter-annual variability and implications for the neutral atmosphere. J. Geophys. Res. 109, doi:10.1029/2003JE002154. E03010.

Bougher, S.W., Bell, J.M., Murphy, J.R., Lopez-Valverde, M.A., Withers, P.G., 2006. Polar warming in the Mars thermosphere: Seasonal variations owing to changing insolation and dust distributions. Geophys. Res. Lett. 32, doi:10.1029/2005GL024059. L02203.

Bougher, S.W., Bell, J.M., Steers, B.M., Keating, G.M., Murphy, J.R., 2007. Winter polar warming in the Mars thermosphere. In: 7th International Conference on Mars, Pasadena, CA, 9–13 July 2007.

Brain, D.A., Bagenal, F., Acuna, M.H., Connerney, J.E.P., 2003. Martian magnetic morphology: Contributions from the solar wind and crust. J. Geophys. Res. 108 (A12), doi:10.1029/2002JA009482. 1424.

Cain, J.C., Ferguson, B.B., Mazoni, D., 2003. An $n = 90$ internal potential function of the martian crustal magnetic field. J. Geophys. Res. 107 (E2), doi:10.1029/2000JE001487. 5008.

Forbes, J.M., Hagan, M.E., 2000. Diurnal Kelvin wave in the atmosphere of Mars: Towards an understanding of "stationary" density structures observed by the MGS accelerometer. Geophys. Res. Lett. 27, 3563–3566.

Forbes, J.M., Bridger, A.F.C., Bougher, S.W., Hagan, M.E., Hollingsworth, J.L., Keating, G.M., Murphy, J.R., 2002. Nonmigrating tides in the thermosphere of Mars. J. Geophys. Res. 107 (E11), doi:10.1029/2001JE001582. 5113.

Fox, J.L., Dalgarno, A., 1979. Ionization, luminosity, and heating of the upper atmosphere of Mars. J. Geophys. Res. 84, 7315–7333.

Fox, J.L., Sung, K.Y., 2001. Solar activity variations of the Venus thermosphere/ionosphere. J. Geophys. Res. 106, 21305–21336.

Haberle, R.M., and 9 colleagues, 1999. General Circulation Model simulations of the Mars Pathfinder atmospheric structure investigation/meteorology data. J. Geophys. Res. 104, 8957–8974.

Joshi, M.M., Hollingsworth, J.L., Haberle, R.M., Bridger, A.F.C., 2000. An interpretation of martian thermospheric waves based on analysis of a general circulation model. Geophys. Res. Lett. 27, 613–616.

Keating, G.M., and 27 colleagues, 1998. The structure of the upper atmosphere of Mars: In situ accelerometer measurements from Mars Global Surveyor. Science 279, 1672–1676.

Keating, G.M., Bougher, S.W., Theriot, M.E., Tolson, R.H., Blanchard, R.C., Zurek, R.W., Forbes, J.M., Murphy, J.R., 2006. Initial Mars upper atmospheric structure results from the accelerometer science experiment aboard Mars Reconnaissance Orbiter. Eos (Fall Suppl.) 87 (52). Abstract P33A-06.

Langlais, B., Purucker, M.E., Mandea, M., 2004. Crustal magnetic field of Mars. J. Geophys. Res. 109, doi:10.1029/2003JE002048. E02008.

Liemohn, M.W., and 49 colleagues, 2006. Numerical interpretation of high altitude photoelectron observations. Icarus 182, 383–395.

Lillis, R.J., Mitchell, D.L., Lin, R.P., Connerney, J.E.P., Acuña, M.H., 2004. Mapping crustal magnetic fields at Mars using electron reflectometry. Geophys. Res. Lett. 31, doi:10.1029/2004GL020189. L15702.

Lillis, R.J., Engel, J.H., Mitchell, D.L., Brain, D.A., Lin, R.P., Bougher, S.W., Acuna, M.H., 2005. Probing upper thermospheric neutral densities at Mars using electron reflectometry. Geophys. Res. Lett. 32, doi:10.1029/2005GL024337. L23204.

Lillis, R.J., Mitchell, D.L., Lin, R.P., Acuña, M.H., 2008a. Electron reflectometry in the martian atmosphere. Icarus 194, 544–561.

Lillis, R.J., Frey, H.V., Manga, M., Mitchell, D.L., Lin, R.P., Acuña, M.H., Bougher, S.W., 2008b. An improved crustal magnetic field map of Mars from electron reflectometry: Highland volcano magmatic history and the end of the martian dynamo. Icarus 194, 575–596.

Lin, R.P., 1979. High spatial resolution measurements of surface magnetic fields of the lunar frontside. Proc. Lunar Sci. Conf. 10 (3), 2259–2264. A80-2367708-91.

Liu, J., Richardson, M.I., Wilson, R.J., 2003. An assessment of the global, seasonal, and inter-annual spacecraft record of martian climate in the thermal infrared. J. Geophys. Res. 108 (E8), doi:10.1029/2002JE001921. 5089.

Lopez-Valverde, M.A., Edwards, D.P., Lopez-Puertas, M., Roldan, C., 1998. Non-local thermodynamic equilibrium in general circulation models of the martian atmosphere. 1. Effects of the local thermodynamic equilibrium approximation on thermal cooling and solar heating. J. Geophys. Res. 103, 16799–16811.

Mazarico, E., Zuber, M.T., Lemoine, F.G., Smith, D.E., 2007. Atmospheric structure of the martian atmosphere near 250 km altitude from Mars Reconnaissance Orbiter radio tracking data. Lunar Planet. Sci. 38, 1715.

Mitchell, D.L., Lin, R.P., Rème, H., Crider, D.H., Cloutier, P.A., Connerney, J.E.P., Acuña, M.H., Ness, N.F., 2000. Oxygen Auger electrons observed in Mars' ionosphere. Geophys. Res. Lett. 27, 1871–1874.

Mitchell, D.L., Lin, R.P., Mazelle, C., Rème, H., Cloutier, P.A., Connerney, J.E.P., Acuña, M.H., Ness, N.F., 2001. Probing Mars' crustal magnetic field and ionosphere with the MGS electron reflectometer. J. Geophys. Res. 106, 23419–23427.

Mitchell, D.L., Lillis, R.J., Lin, R.P., Connerney, J.E.P., Acuña, M.H., 2007. A global map of Mars' crustal magnetic field based on electron reflectometer. J. Geophys. Res. 112 (E1), doi:10.1029/2005JE002564. E0100.

Nier, A.O., McElroy, M.B., 1977. Composition and structure of Mars' upper atmosphere—Results from the neutral mass spectrometers on Viking 1 and 2. J. Geophys. Res. 82, 4341–4349.

Purucker, M.E., Ravat, D., Frey, H., Voorhies, C., Sabaka, T., Acuña, M.H., 2000. An altitude-normalized magnetic map of Mars and its interpretation. Geophys. Res. Lett. 27, 2449–2452.

Smith, M.D., 2004. Inter-annual variability in TES atmospheric observations of Mars during 1999–2003. Icarus 167, 148–165.

Smith, D.E., and 24 colleagues, 2001. Mars Orbiter Laser Altimeter: Experiment summary after the first year of global mapping of Mars. J. Geophys. Res. 106, 23689–23722.

Smith, M.D., Conrath, B.J., Pearl, J.C., Christensen, P.R., 2002. Thermal emission spectrometer observations of martian planet-encircling dust storm 2001A. Icarus 157, 259–263.

Whaler, K.A., Purucker, M.E., 2005. A spatially continuous magnetization model for Mars. J. Geophys. Res. 110 (E9), doi:10.1029/2004JE002393. E09001.

Wilson, R.J., 2002. Evidence for nonmigrating thermal tides in the Mars upper atmosphere from the Mars Global Surveyor accelerometer experiment. Geophys. Res. Lett. 29 (7), doi:10.1029/2001GL013975. 1120.

Withers, P., 2003. Tides in the martian atmosphere and other topics. Ph.D. thesis, Univ. of Arizona, Tucson.

Withers, P., 2006. Mars global surveyor and Mars Odyssey accelerometer observations of the martian upper atmosphere during aerobraking. Geophys. Res. Lett. 33, doi:10.1029/2005GL024447. L02201.

Withers, P., Bougher, S.W., Keating, G.M., 2003. The effects of topographically-controlled thermal tides in the martian upper atmosphere as seen by the MGS accelerometer. Icarus 164, 14–32.